Journal Pre-proof

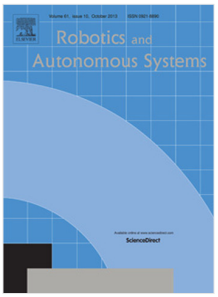

On planar self-folding magnetic chains: Comparison of *Newton-Euler* dynamics and internal energy optimisation

T.H. Fass, Guangbo Hao, Pádraig Cantillon-Murphy

PII: S0921-8890(20)30441-3
DOI: https://doi.org/10.1016/j.robot.2020.103601
Reference: ROBOT 103601

To appear in: *Robotics and Autonomous Systems*

Received date : 17 November 2019
Revised date : 11 May 2020
Accepted date : 6 July 2020

Please cite this article as: T.H. Fass, G. Hao and P. Cantillon-Murphy, On planar self-folding magnetic chains: Comparison of *Newton-Euler* dynamics and internal energy optimisation, *Robotics and Autonomous Systems* (2020), doi: https://doi.org/10.1016/j.robot.2020.103601.

Highlights

On planar self-folding magnetic chains: Comparison of *Newton-Euler* dynamics and internal energy optimisation

T.H. Fass, Guangbo Hao, Pádraig Cantillon-Murphy

- Characterisation and implementation of planar magnetic chains at bench-top scale to investigate magnetic self-folding
- Analysis of folding prediction methods for planar self-folding magnetic chains, with special focus on energy minimization methods and *Newton-Euler* dynamics
- Novel analytical interpretation and numerical application of *Newton-Euler* equations for the prediction of planar self-folding magnetic chains
- Demonstration of potential for self-folding magnetic chains for applications in minimally invasive surgery

On planar self-folding magnetic chains: Comparison of *Newton-Euler* dynamics and internal energy optimisation

T.H. Fass[a,b,*], Guangbo Hao[a,b], Pádraig Cantillon-Murphy[a,b]

[a] *Tyndall National Institute, Lee Maltings Complex Dyke Parade, Cork, T12 R5CP, Ireland*

[b] *School of Engineering, College Rd, University College, Cork, T12 K8AF, Ireland*

Abstract

Within the wide field of self-assembly, the self-folding chain has the unique capability to pass through narrow openings, too small for the assembled structure, yet consists in one connected body. This paper presents a novel analytical framework and corresponding experimental setup to quantify the results of a self-folding process using magnetic forces at the centimetre-scale, with the aim to put experimental results and prediction methods in the context of surgical anchoring and therapy. Two possibilities to predict the folding of a chain of magnetic components in 2D are compared and investigated in an experimental setup. Folding prediction by system *Coulomb* energy, neglecting folding dynamics, is compared with a simulation of the system dynamics using a novel approach for 2D folding chains, derived from the *Newton-Euler* equations. The presented algorithm is designed for the parallel computation architecture of modern computer systems to be easily applicable and to achieve an improved simulation speed. The experimental setup for the *self-folding* chain used to validate the simulation results consists of a chain of magnetic components where movement is limited to one plane and the chain is agitated by the magnetic forces between the chain components. The folding process of the experimental setup is validated for its stability and predictability under different deployment modes. Finally, the results are discussed in light of the folding prediction of longer chains. The implications of the presented findings for a 3D folding chain are dis-

*Corresponding Author

cussed together with the challenges to apply the novel dynamics simulation algorithm to the 3D case. The work clearly demonstrates the potential for this novel approach for complex self-folding applications such as magnetic compression anastomosis and anchoring in minimally invasive surgery.

Keywords: Magnetic self-folding chain, self-assembly, *Newton-Euler* dynamics, magnetic surgery

1. Introduction

Self-assembly, as a branch of robotics, seeks to enable machines and devices to assemble themselves in order to allow for improved assembly methods or a flexible change of functionality [1]. A sub group of self-assembly is the self-folding, where a chain of components folds to specific shapes [2]. The biological model par excellence for this is *protein biosynthesis*.

Protein biosynthesis is a process in every living cell in which a chain of amino acid molecules folds into complex 3D structures called proteins [3]. The process is able to produce a wide range of shapes, depending on the sequence of amino acids along the chain. Understanding and predicting the principle of self-folding chains could not only lead to engineering of proteins, but the process could be translated to origami robots[4] across multiple scales, capable of mimicking a wide range of shapes and tools. One particular application of interest is to apply self-folding chains, with magnetism as the processes driving force, for uses in minimally invasive surgery, exploiting the property of magnetic self-folding chains to pass through narrow deployment ports. During surgery, a chain of magnetic components could be fed through a catheter [5, 6] to be deployed in a otherwise difficult to reach orifice. After deployment the chain assembles itself as a surgical tool or therapeutic device larger than the catheter or port used to deploy them. Self-assembled tools might be an anastomoses ring [7] or magnetic anchor [8]. In order to fold the chain into a specific shape, reliable prediction of the folding process is necessary.

Many mathematical approaches for the prediction of self-folding [9] and rigid body dynamics [10] exist. The current work explores a concept for simple 2D magnetic self-folding chains mimicking the capability of *protein biosynthesis* for a self-assembling process and explores two different approaches

to predict the folding of the chain. In this paper the folding process is limited to a 2D plane for controllability.

A simple 2D magnetic folding chain has been constructed and its folding behaviour analysed for repeatability and real time dynamics. These experimental results are used to validate numerical prediction methods. The real-time dynamics simulation is based on a novel interpretation of *Newton-Euler* dynamics, that seeks to offer an alternative to existing rigid body dynamics algorithms. By expressing the dynamics of a planar chain in a single vectorised differential algebraic equation, the resulting algorithm allows a convenient implementation that utilises parallel computation architecture. The dynamics simulation, is compared to experimental results as well as the prediction of the folding comparing the free energy of all possible foldings of the system. As the chains discussed in this paper fold themselves into assembled structures without coordinated manipulation from outside driving forces, they may be considered self-assembling [1]. However, for self-assembly to reliably fold into useful structures, it has to be predictable. As magnets are scalable and might produce high forces in comparison to their weight and size, they are used as actuators in many applications of self-assembling systems [11].

Here we discuss existing ways to predict this process of self-folding in order to validate the results of the paper. The movement of a chain of components can be predicted in one of two different ways:

(1) Analysing the dynamics of the system, allows to predict the steps of movement and follow it to its state of interest.
(2) Directly predicting possible states of interest and picking the one most likely to occur.

In both cases, a particular state of interest is where the system is in equilibrium and the components stop moving with respect to each other.

As all systems drive toward their minimum of internal free energy [12], the folding chain has such states of interest where the internal energy of the system reaches a global or local minimum. These states of interest, where the components of the chain stop moving with respect to each other, are referred to as *folded states* in this paper. By its definition, these state of interest are static and, in the case of a folding chain, the internal free energy of the system might be defined by potential energy resulting from forces acting

on the system, such as gravity, or forces acting within the system, such as magnetic attraction or repulsion. If the internal energy of the system can be calculated, its minimum value can be found and, with it, the folded states of the system, without regarding the movement to reach this state. Depending on the system, this approach may be more efficient than calculating the system dynamics and is often used in the prediction of protein folding [3]. A real system, however, might fold into a local minimum of internal free energy instead of the global minimum. Different approaches exist to compensate for such events. Analysing the dynamics of the system gives a better understanding of the folding process and predicts in which minima of free energy the system may lie [13].

The dynamics of a system are commonly characterised by the *Newton-Euler* equation or the *Euler-Lagrange* equation. The *Newton-Euler* equation is based on an equilibrium of forces F and acceleration a acting on a body with the mass m;

$$ma = F \tag{1}$$

and the equilibrium of torques τ and angular acceleration α of the same body with inertia I can be described as;

$$I\alpha = \tau + \frac{\partial \alpha}{\partial t} \times I \frac{\partial \alpha}{\partial t} \tag{2}$$

In the 2D case $\frac{\partial \alpha}{\partial t} \times I \frac{\partial \alpha}{\partial t} = 0$ and Equation (2) is reduced to;

$$I\alpha = \tau \tag{3}$$

The *Euler-Lagrange* equation (second kind) is expressed as;

$$\frac{\partial}{\partial t} \frac{\partial L}{\partial \dot{\xi}_i} - \frac{\partial L}{\partial \xi_i} = 0 \tag{4}$$

where $L = T - V$ is the difference of the kinetic energy T and the potential energy V. ξ_i are the generalised coordinates of the system and $\dot{\xi}_i$ are the generalised velocities. *Silver 1982* [14] attempts a comparison between the *Euler-Lagrange* and the *Newton-Euler* approach and shows that both are comparable in the possible representation of rotation in the system and both may potentially be used recursively to compute the dynamics of a system.

The system dynamics can be efficiently computed recursively with the *Articulated-Body Algorithm*[15], by computing the forces in the links, component by component. Due to the use of *Graphics Processing Units* (GPU), multi core processors and the *Single Instruction Multiple Data* (SIMD) model [16] modern computers are able to process multiple operations simultaneously and significantly increase computational speed. A different class of algorithms is necessary to utilise this potential for parallel computation architecture, such as with the *Divide and Conquer* algorithm [17] that is based on the *Newton-Euler* equations. *Chadaj 2017* [18] presents a implementation of *Divide and Conquer* algorithm for the *Hamilton* equations to utilise parallel computation capability. These algorithm separate the chain in segments that are computed simultaneously. Another possibility is the vectorisation of the algorithm, where the dynamics of the system are represented in a set of vector equations that allow for the computation of system dynamics for all components of the system simultaneously. GPUs and the SMID model are particularly efficient in regards to vector computations [16]
K. Chadaj 2017 [18] presents a recursive algorithm suitable for parallel computation is based on *Euler-Lagrange* equations. *A. Stokes1996* [19] and *P.C. Müller 1992* [20] describe two vectorised approaches to the *Euler-Lagrange* kinematics.

A vectorised approach to *Newton-Euler* dynamics, as presented by *P.C. Müller 1992* [20] and *R. Lathrop 1985* [21], is generalised for any composite of rigid bodies to compute the forces in the system and associated system dynamics [22].

2. Self-Folding Magnetic Chain Design

While the preceding approaches of describing the dynamics of multi-rigid-body systems based on *Newton-Euler* or *Euler-Lagrange* are applicable to general folding chains, they are applied and tested in this paper for a chain folding itself driven by magnetic forces between the components on a plane. This section describes the analysed setup.

Each chain component is a square casing and is connected to the previous and the next component by a wire as seen in Figure 1. A cotton, polyester wire with high bending elasticity and a low axial elasticity was chosen, to best approximate a revolute joint between the components. The dimension

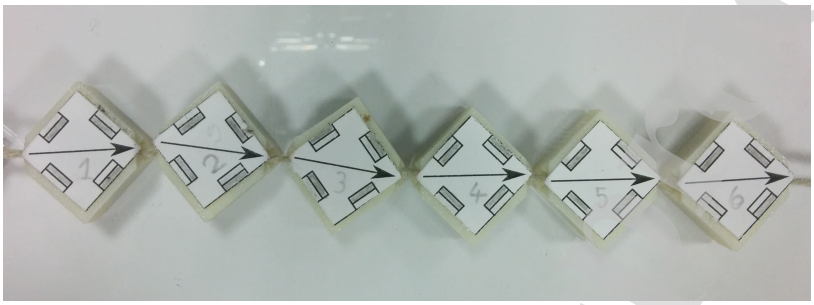

Figure 1: Experimental setup of the 2D self-folding magnetic chain

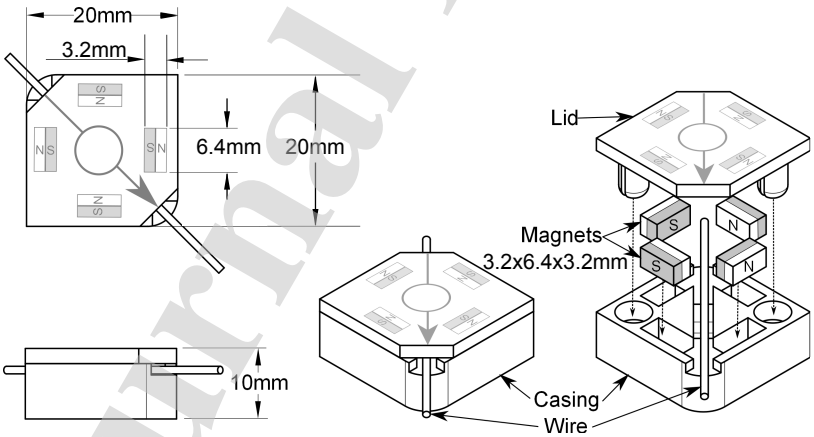

Figure 2: Single component of the 2D self-folding magnetic chain, investigated in this work. Orientation of the magnet is displayed on the lid of the casing.

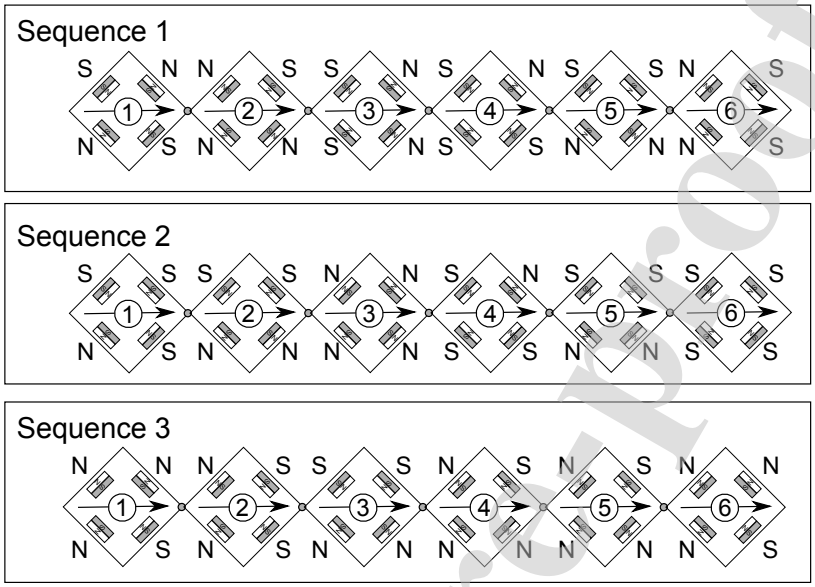

Figure 3: Tested sequences of components in 2D self-folding. "N" and "S" indicate the magnet polarisation relative to outward faces.

of each component can be seen in Figure 2. The casings were designed to allow an exchange of the magnets and approximate the behaviour of an ideal chain. In the present work, the degree of freedom is defined as the angle between each chain component. The chain folds on a flat, low friction surface due to the forces acting between the magnets. All movement is normal to the surface and is restricted to two dimensions. Gravity is only applied in the friction model. Each component contains one magnet on each of the four faces, having either its north or south side closest to the outer face as seen in Figure 2.

The chain is defined by the sequence of casing components and how their magnets are oriented relative to outward faces. For components containing four magnets as seen in Figure 2. This results in $2^4 = 16$ different combinations of magnetic orientation in each casing component, resulting in 16^n different sequences of chain components, for a chain with n components. This setup allows for an easy implementation of different sequences by manually exchanging the magnets, while the limitation of the movement to a plane increases controllability and allows for a better observation and analysis of

the chain movement.

The given experimental setup supports a chain length of up to 6 components. In experiments with more components the magnets at this scale does not provide sufficient force to overcome surface friction and the folding process does not occur. During the folding process the *self-folding* chain is assumed to minimise its internal free energy. The chain changes from an unfolded high energy state to a folded low energy state. This low energy state might not be the minimal possible energy of the system but a local minimum. The free energy of the chain is the sum of kinetic and potential energy. In the folded position the chain is in rest and the kinetic energy is zero. Therefore, only the potential energy defines the folded states of the chain. However, during the folding process the inertia of the chain might influence how the fold occurs and which energy minimum is reached. The experimental setup allows for the specific construction of number and shape of possible folding shapes and the corresponding energy minima. It is of interest what the effect of multiple energy minima has on the reliability of the folding process as well as the possible effect of the chain inertia. Three distinct chain types were investigated to quantify the folding process:

(1) The chain has multiple stable states, resulting in multiple local minima of the internal free energy.
(2) The chain has multiple stable states, resulting in local minima of the internal free energy, one of which requires the least possible lateral displacement of the components.
(3) The chain is constructed to only support one stable state.

A state is considered stable if it is fully folded and no two magnets with the same polarity face toward each other. Therefore, for each chain type case, a representative exemplar of a distinct chain as displayed in Figure 3 was build and analysed. In the following sections, a folding prediction search based on minimisation of internal energy is compared to a novel interpretation of the *Newton-Euler* equations to simulate the dynamics of a magnetic chain, followed by presentation of an experimental setup of self-folding magnetic chains. Finally, simulated results are compared to the experimental outcomes.

3. Magnetic Point Charge Model

In this paper, the magnets are simulated with the point charge model, where each magnetic face is represented by a set of point charges. These point charges are introduced based on the magnetic charge analogy to electric charges but with no physical significance [23]. Each magnet is approximated by $2h$ point charges of equal absolute charge $|q|$ and with h point charges equally distributed over each north and south polarised surface. The forces acting between the magnets are approximated by the sum of forces acting between the point charges. The force acting on the k^{th} magnetic point charge with respect to the l^{th} magnetic point charge, with the charges q_k and q_l, is defined by *Coulomb's* law for magnetic charges [23]:

$$\vec{\mathbf{F}}_{mag\,kl} = (\vec{\mathbf{x}}_l - \vec{\mathbf{x}}_k)\frac{\mu_0}{4\pi}\frac{q_k q_l}{|\vec{\mathbf{x}}_l - \vec{\mathbf{x}}_k|^3} \tag{5}$$

where $\vec{\mathbf{x}}_k$ and $\vec{\mathbf{x}}_l$ are the positions of the respective point charges and $\mu_0 = 4\pi \cdot \not{}10^{-7}\,\mathrm{Am/T}$ is the constant magnetic permeability of free space.

The potential energy in the system wich is defined by magnetic interaction as a function of point charge position can be expresed as;

$$U(\vec{\mathbf{x}}_1, .., \vec{\mathbf{x}}_{n_q}) = \sum_{k}^{n_q}\sum_{l|k\neq l}^{n_q}\frac{\mu_0}{4\pi}\frac{q_k q_l}{|\vec{\mathbf{x}}_l - \vec{\mathbf{x}}_k|} \tag{6}$$

with $U(\vec{\mathbf{x}}_1, .., \vec{\mathbf{x}}_{n_q})$ being the *Coulomb* energy of the system, given by the double summation over all n_q point charges with $k \neq l$.
The absolute charge $|q| = |q_k| = |q_l|$ was considered equivalent for all magnetic charges, as is typically the case in a magnetic system.

4. Energy Minimisation Method

In this section the calculation of internal free energy for a magnetic chain is discussed and used to identify possible minima of internal free energy, to attempt a prediction of the results of the folding process [12].

The approach is applied to the chains described in Figure 3. Only fully folded chains are considered states of interest. A chain is fully folded if none of the components is moving with respect to each other. As such, the kinetic energy of the system is neglected and the internal free energy of the static system is defined only by the potential energy resulting from the magnetic

force between the magnets, presented in (6). As only static states of the system are analysed, friction is neglected in this calculation.

For this simulation the residual flux density for each magnet was estimated as 0.6 T , measured with a flux meter on the surface of the magnet, resulting in a point charge magnitude of

$$q_i = \pm \frac{17.1892\,\mathrm{Am}}{2h} \tag{7}$$

No significant change in the folding prediction was observed for $h \geq 3$ point charges per polarised surface as subsequently shown by the comparison to the experimental setup. Therefore each polarised magnetic surface was initially approximated with $h = 3$ point charges, corresponding to a magnetic point facet area of 6 mm^2. The dimension of each component can be seen in Figure 2.

Input:$(\phi_{r\,i}, .., \phi_{r\,n}) \in \mathbb{R}^n$
(i) Update component position depending on $(\phi_{r\,i}, .., \phi_{r\,n})$
(ii) Update charge position $(\vec{\mathbf{x}}_1, .., \vec{\mathbf{x}}_{n_q})$ depending on component position.
(iii) solve Equation (6) $U(\vec{\mathbf{x}}_1, .., \vec{\mathbf{x}}_{n_q}) = \sum_k^{n_q} \sum_{l|k\neq l}^{n_q} \frac{\mu_0}{4\pi} \frac{q_k q_l}{|\vec{\mathbf{x}}_l - \vec{\mathbf{x}}_k|}$
Output: *Coulomb* energy $U \in \mathbb{R}$

Figure 4: Pseudo code describing the cost-function for the *Coulomb*-energy

The cost function that is to be minimised is the internal potential energy of the system. In the idealised planar case we assume the potential energy is equivalent to the *Coulomb* energy presented in Equation (6). Point charges with a large distance between them might have an insignificant influence on the coulomb energy of the system, however as the computational effort of the analysed systems is low, no distance threshold was implemented to exclude point charges from computation. The variables of interest are the relative angles $\phi_{r\,i}$ between adjacent components, is fixed to a position relative to one of the components where the magnet surface is located in the experimental setup. Therefore, the position of each point charge is fully defined by the relative angle between components and we therfore define the cost function as a function of the angles between the components as seen in Figure 4.

(i) prepare list of results
(ii) for all possible states of $\phi_{r\,i} \in \{\pi/2, 0, -\pi/2\}$
(iii) –calculate distance between component centres
(iv) –if all centre distances are greater than 3 mm
(v) —calculate *Coulomb* energy with cost function (4)
(vi) —add *Coulomb* energy and corresponding input $(\phi_{r\,1}, .., \phi_{r\,n})$ to list of results
(vii) Sort list of results for minimum *Coulomb* energy

Figure 5: Pseudo code describing the full search space optimisation of a magnetic self-folding chain

This paper does not seek to improve possible optimisation methods but rather seeks to place possible results of optimisation into the context of experimental folding and folding dynamics for magnetic chains. Therefore, in order to eliminate the possibility of missing a state of interest, the internal energy of all possible states of interest of the chains displayed in Figure 3 were taken into account. Due to the geometry of the components, only relative angles of $\phi_{r\,i} \in \{\pi/2, 0, -\pi/2\}$ could lead to folded states, where $\phi_{relative} = 0$ corresponds to the initial position seen in Figure 3. This results in $3^6 = 729$ states, for $n = 6$ components. Under certain conditions other stable states are possible, for example if a component is repelled and attracted at the same time by closely neighbouring components. This is more likely to occur as the number of components increases and the closer they are located. In the experimental setup, the chain was mechanically prevented from these states to occur as they unnecessarily complicate the experimental setup. To filter these unrealistic states, all states where the centres of any two components were less than 3 mm apart are excluded from computation. This includes all the states where two components overlap and that therefore can not occur in the experimental setup. Therefore, the optimisation was executed in a discrete search space of $\phi_{r\,i} \in \{\pi/2, 0, -\pi/2\}$ and with the constraint to exclude states with overlapping tiles. The corresponding pseudocode is displayed in Figure 4.

In a clinical application, the self-folding magnetic chain might be deployed via a catheter or needle [7]. In this case, the chain might not fold all

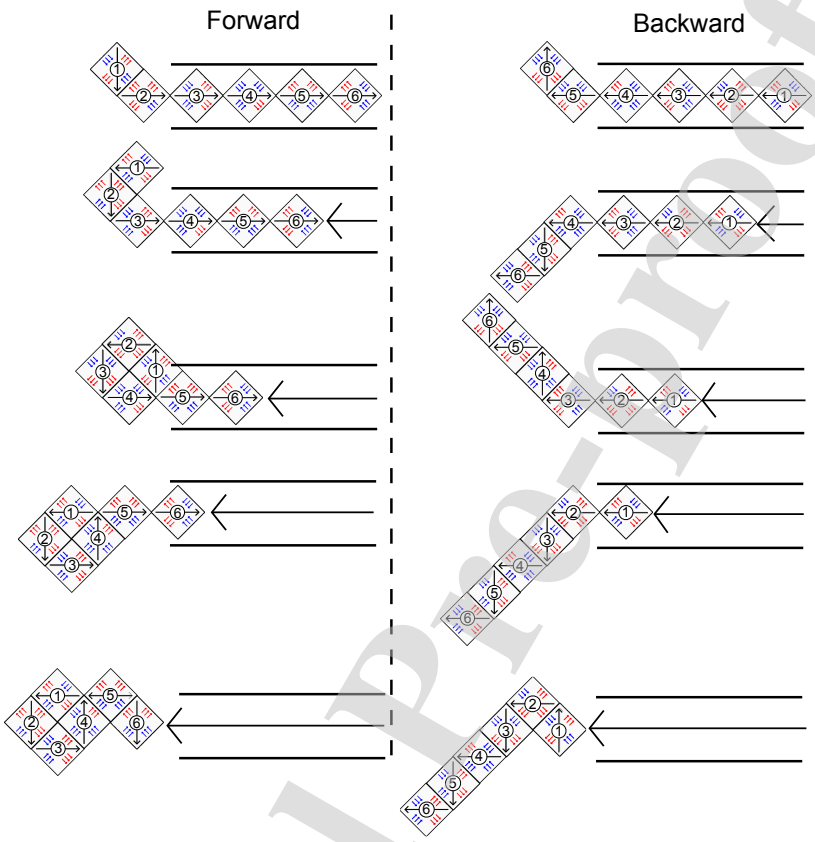

Figure 6: Component by component energy minimisation to approximate *tube-feed* deployment mode of sequence 1, in forward (left) and backward (right) deployment.

components at a time as the deployment catheter causes the components to fold sequentially as they exit the catheter. If the folding speed is higher than the deployment speed, this might cause the chain components to fold one at a time. Therefore, we assume a deployment speed slower than the folding speed to achieve a clear differentiation between three deployment modes:

(i) *Free-fold*: All components of the chain fold at the same time. All 729 possible folding states are tested.

(ii) Forward *tube-feed*: The chain is considered to fold one relative angle between components at a time. Energy minimisation prediction is conducted for the whole chain, one degree of freedom at a time, starting with the angle between the first and second component, as seen in

Figure 6.

(iii) Backward *tube-feed*: The chain is considered to fold one relative angle between components at a time. Energy minimisation prediction is conducted for the whole chain, one degree of freedom at a time, starting with the angle between the last and second to last component, as seen in Figure 6.

4.1. Results

Figure 7 shows the calculated *Coulomb* energy for the 5 folded states with the least *Coulomb* energy, for each chain sequence shown in Figure 3. The results show that only sequence 3 provides one stable folded state. Furthermore, it shows, that sequence 1 and 2 feature more than one possible stable state, with associated local minima which the chain could fold into.

The result show that different sequences can stably fold into the same shape, as S1A and S3A have equivalent outlines, yet different *Coulomb* energy score results. As (6) shows, the potential energy between two equally polarised point charges, repelling each other, increases the sum of *Coulomb* energy in the system, whereas two opposite polarised point charges reduce it. The *Coulomb* energy is computed between all point charges, including those point charges that are located in the same component. As the relative distance between point charges in the same component does not depend on the position to other components, these add a sequence specific constant to the *Coulomb* energy score. As a result, the *Coulomb* energy score of a folded chain might be positive as seen for Sequence 2 and yet represent a stable folding state.

The difference in *Coulomb* energy between S2B and S2A is 55.89% with just one of the relative angles between the components being different. S2B in comparison to S2C has two different angles and a change in *Coulomb* energy of just 8.75%. Therefore the change of *Coulomb* energy is not directly proportional to the change in shape.

The results also support the assumption that, as the *Coulomb* energy of stable foldings decreases, the more faces with opposite polarity are in contact with each other and as a result, the more compact the shape is.

The *tube-feed* simulation shows that the chain under the conditions of a *tube-feed* does not necessarily fold into its global minima of internal free en-

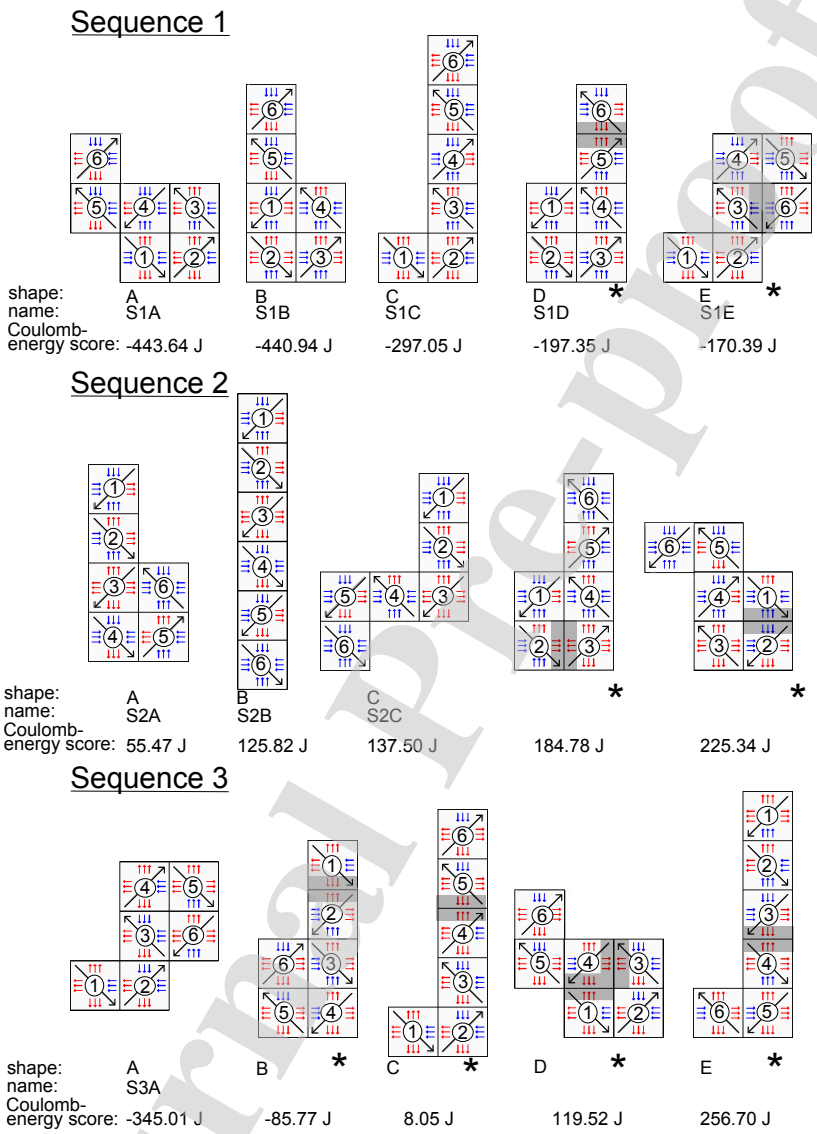

Figure 7: *Coulomb* energy minimisation results. Short arrows show direction of magnetic polarisation. Base of arrow marks the position of a positive charge, whereas the tip marks the position of a negative charge. Long arrows show chain direction. Folded shapes marked with * contain a conflict, highlighted in the drawing, meaning two surfaces of the same polarisation in contact with each other.

ergy. The *tube-feed* energy minimisation prediction results for each sequence

are summarised in Table 1.

Table 1: Component by component energy minimisation results, for the *tube-feed* deployment mode.

energy minimisation simulation	predicted shape
sequence 1; forward	S1A
sequence 1; backward	S1C
sequence 2; forward	S2B
sequence 2; backward	S2B
sequence 3; forward	S3A
sequence 3; backward	S3A

As sequence 3 only supports one possible stable state, it is to be expected that both forward and backward *tube-feed* simulation result in the shape S3A. Sequence 1 shows different folding shapes depending on deployment direction, as different states might be more favourable depending on deployment direction when only one component at a time folds. However, sequence 2 features multiple stable states but only folds into shape S2B during *tube-feed* simulation. As shape S2B is a straight line of components, the calculation of *Coulomb* energy component per component remains constant whether if the simulation starts with the first or the last component. The reason for this can be described by comparing shape S2A and S2B. The only difference between these two shapes is the angle between component 4 and 5. The connection between component 3 and 6 gives shape S2A two more magnetic surfaces in contact with each other than all other stable states and as a result shape S2A is the global minima of all states of interest of sequence 2. However, in the forward *tube-feed* scenario when the angle between component 4 and 5 is optimised, component 6 is still in the tube and cannot come in contact with component 3. As a result, a fold in the opposite direction is more favourable. Similarly, the shape S2B is more favourable during the backward *tube-feed* scenario.

The backward *tube-feed* prediction of Sequence 1 suggests that the chain does not necessarily fold into its global minima, depending on the deployment mode. In conclusion the energy minimisation method might be modified such as in the *tube-feed* prediction to compensate for some deployment modes.

However, the internal energy of the system is computed by assuming the system to be static and depending on the movement speed, the dynamics of the system might cause a fold into an unpredicted minimum of internal energy.

5. Dynamic Simulation

In light of the evident shortcomings of the energy minimisation approach, this section formulates the vectorised forward dynamics of a generalised 2D magnetic chain. The forward dynamics use the forces acting on the chain as an input and describe the resulting chain movement.

As both the *Newton-Euler* and the *Euler-Lagrange* methods are capable of describing the dynamics of a chain, it is important to determine which one leads to the computationally more efficient algorithm, to accurately compute the dynamics of longer chains. In the presented case of a magnetic folding chain, the degrees of freedom are the folding angles between the chain components. Applying the *Euler-Lagrange* Equation (4) directly, the potential energy and therefore the *Coulomb* energy given in Equation (6) is derived by all degrees of freedom. *J. Luh 1980* [24] proposed the introduction of pseudo accelerations to compensate for gravitational forces. However, the forces acting on each component in a self-folding magetic chain and the potential energy in the system depend on their distance to other components in the chain as seen in Equations (5) and (6), whereas this distance is dependent of the folding angles between chain components. The magnetic forces and the potential energy in the presented system dependent on all folding angles defining the system. The resulting equation gets super-linearly more complex with a increasing number of chain components.

In contrast to the *Euler-Lagrange* algorithm is the consideration of forces in the *Newton-Euler* more convenient. In the 2D case as it is analysed here, the *Newton-Euler* equations are expressed in their simplified Equations (1) and (3) and therefore chosen to formulate a single vectorised differential equation describing the dynamics of a planar folding-chain with any number of components and thus allowing for a convenient use vector computation libraries, that are able to utilise the advantages of SIMD architecture.

Table 2: Table of symbols

sym.	description	set
n	number of components in the chain	$\in \mathbb{N}$
m_i	mass of the i^{th} component	$\in \mathbb{R}$
I_i	inertia with respect to the centre of mass of the i^{th} component	$\in \mathbb{R}$
$z_{\mathrm{m}\ i}$	position of the i^{th} centre of mass with respect to the world frame	$\in \mathbb{C}$
$\vec{\mathbf{z}}_m$	$= [z_{m1}, .., z_{mn}]^t$	$\in \mathbb{C}^n$
v_{mi}	velocity of the i^{th} centre of mass with respect to the world frame	$\in \mathbb{C}$
$\vec{\mathbf{v}}_m$	$= (v_{m1}, .., v_{mn})^t$	
a_{mi}	acceleration of the i^{th} centre of mass with respect to the world frame	$\in \mathbb{C}$
$\vec{\mathbf{a}}_m$	$= [a_{m1}, .., a_{mn}]^t$	
r_{li}	complex vector pointing from link between component i and $i-1$ to center of mass of i^{th} component	$\in \mathbb{C}$
r_{ci}	complex vector pointing from center of mass of i^{th} component to the link between component i and $i+1$	$\in \mathbb{C}$
ϕ_i	orientation of i^{th} component with respect to the world frame	$\in \mathbb{R}$
$\vec{\boldsymbol{\phi}}$	$= [\phi_1, .., \phi_n]^t$	$\in \mathbb{R}^n$
ω_i	angular velocity of i^{th} component with respect to the world frame	$\in \mathbb{R}$
$\vec{\boldsymbol{\omega}}$	$= [\omega_1, .., \omega_n]^t$	$\in \mathbb{R}^n$
$\dot{\omega}_i$	angular acceleration of i^{th} component with respect to the world frame	$\in \mathbb{R}$
$\dot{\vec{\boldsymbol{\omega}}}$	$= [\dot{\omega}_1, .., \dot{\omega}_n]^t$	$\in \mathbb{R}^n$
f_{gi}	generalised force acting on the i^{th} component	$\in \mathbb{C}$
$\vec{\mathbf{f}}_g$	$= [f_{g\,1}, .., f_{g\,n}]^t$	$\in \mathbb{C}^n$
f_{li}	force acting on the joint between the component i and $i-1$	$\in \mathbb{C}$
$\vec{\mathbf{f}}_l$	$= [f_{l\,1}, .., f_{l\,n}]^t$	$\in \mathbb{C}^n$
t_{gmi}	generalised torque acting on the center of massof the i^{th} component	$\in \mathbb{R}$
$\vec{\mathbf{t}}_{gm}$	$= [t_{gm\,1}, .., t_{gm\,n}]^t$	$\in \mathbb{R}^n$

5.1. Vectorised complex 2D dynamics of a chain

This work seeks to analyse the dynamics of planar folding chain. In contrast to the 3D case, each component in the chain has one degree of freedom, the folding angle. As such, to make use of parallel computation, a vectorised differential equation was devised that would express angular acceleration of all chain components in the form

$$\dot{\vec{\omega}} = \mathrm{F}(\vec{\omega}, \vec{\phi}, \vec{\mathbf{f}}, \vec{\tau}) \tag{8}$$

Expressing the dynamics in such a form allows for an convenient implementation with common vector computation libraries, enabling a convenient utilisation of parallel computation architecture, including SIMD. The vectorisation library used in this work is *NumPy*. This section shows how the function $\mathrm{F}(\vec{\omega}, \vec{\phi}, \vec{\mathbf{f}}, \vec{\tau})$ might be acquired from the *Newton-Euler* equations. Each component of the chain, with index $i \in [1, .., n]$ is characterised as one rigid body with a mass m_i and I_{mi} is the inertia with respect to the centre of mass. For ease of trigonometric notation and due to their convenient representation of 2D rotations, complex numbers were used to express coordinates and rotations in this work. The *Cartesian* coordinates of the vector $\vec{\mathbf{p}} = [p_x, p_y]^t$ are represented by complex numbers of the form $z = p_x + \mathrm{j}p_y$, with $\mathrm{j} = \sqrt{-1}$. The imaginary and real part of these complex numbers represent orthogonal coordinates in a *Cartesian* coordinate system as shown in Figure 8. The chain is considered to have n components. The position of each component in the system is dependent on the angles of the components with respect to the world frame. For the i^{th} component, this angle is named ϕ_i. All angles are the degree of freedom of the system, represented by the vector $\vec{\phi} = [\phi_1, .., \phi_n]$ defining the whole system at time-point t. Absolute angles were chosen to eliminate the need for coordinate transformations and a direct application of ϕ_i and ω_i into Equation 3.
Table 2 shows an overview of all variables and constants used in the presented equations. The first component of the chain with the index 1 is considered to be connected to the world frame by a rotational joint, as seen in Figure 8. The last component of the chain with the index n is considered to be only connected to the component with the index $n-1$, as seen in Figure 8.

The complex representative of the vector from the link connecting component with indices i and $i-1$ to the center of mass of the i^{th} component is labelled r_{li}, as shown in Figure 8. r_{ci} represents the complex vector from the

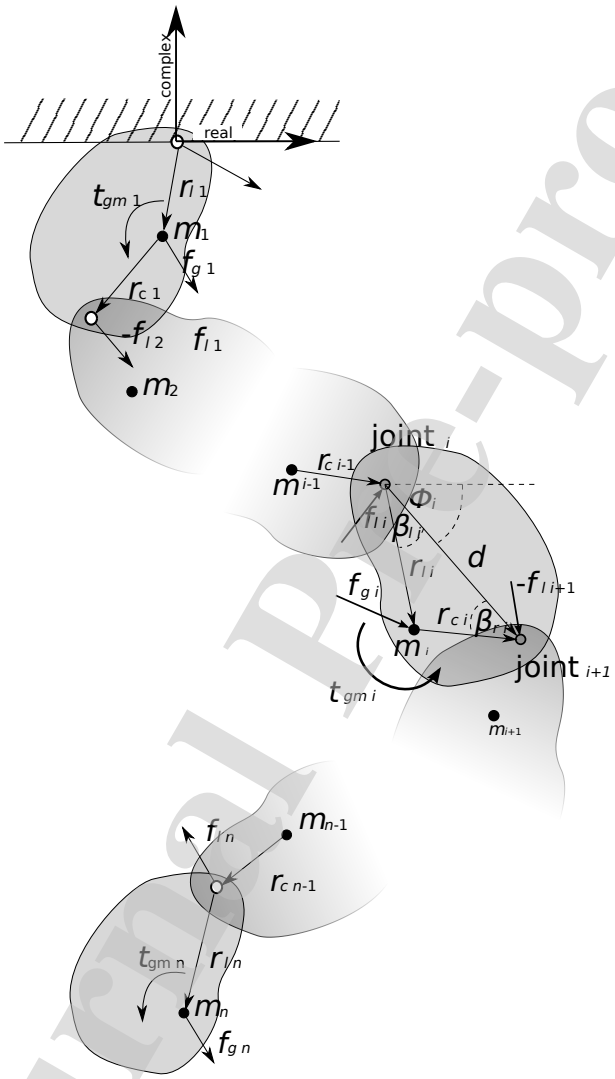

Figure 8: Free force diagram of planar folding chain.

i^{th} center of mass to the link connecting the i^{th} component to the component with the index $i+1$. Consequently d_i is the complex representation of the vector from one link of the i^{th} component to its other link. As d_i, r_{li} and r_{ci}, all belong to the same rigid body, where their position and orientation with respect to each other is constant over time, these might be defined as

$$d_i = |d_i|\mathrm{e}^{\mathrm{j}\phi_i} = r_{li} + r_{ci} \tag{9}$$

$$r_{li} = |r_{li}|\mathrm{e}^{\mathrm{j}(\phi_i+\beta_{li})} \tag{10}$$

$$r_{ci} = |r_{ci}|\mathrm{e}^{\mathrm{j}(\phi_i-\beta_{ri})} \tag{11}$$

with e being *Euler's* number. As $|r_{li}|$, $|r_{ci}|$, β_{li} and β_{ri} are constant in time , therefore the first and second derivative of r_{li}, r_{ci} derived by time t are [25]:

$$\frac{\partial r_{li}}{\partial t} = \dot{r}_{li} = \mathrm{j}r_{li}\dot{\phi}_i = \mathrm{j}r_{li}\omega_i \tag{12}$$

$$\frac{\partial r_{ci}}{\partial t} = \dot{r}_{ri} = \mathrm{j}r_{ci}\dot{\phi}_i = \mathrm{j}r_{ci}\omega_i \tag{13}$$

and

$$\frac{\partial^2 r_{li}}{\partial t^2} = \ddot{r}_{li} = \mathrm{j}r_{li}\dot{\omega}_i - r_{li}\omega_i^2 \tag{14}$$

$$\frac{\partial^2 r_{ci}}{\partial t^2} = \ddot{r}_{ri} = \mathrm{j}r_{ci}\dot{\omega}_i - r_{ci}\omega_i^2 \tag{15}$$

Note that the derivation with respect to time t of any variable p is noted as $\frac{\partial p}{\partial t} = \dot{p}$ and $\frac{\partial^2 p}{\partial t^2} = \ddot{p}$.
The position of the i^{th} components centre of mass in relation to the previous components centre of mass, for all $i \in [2, .., n]$, can be described as

$$z_{mi} = z_{mi-1} + r_{ci-1} + r_{li} \tag{16}$$

Using (15) to twice differentiate (16) by times, the corresponding acceleration of the i^{th} center of mass, for all $i \in [2, .., n]$, may be expressed as

$$\begin{aligned} a_{mi} = \ddot{z}_{mi} &= \ddot{z}_{mi-1} + \ddot{r}_{ri-1} + \ddot{r}_{li} \\ &= a_{mi-1} + \mathrm{j}r_{li}\dot{\omega}_i - r_{li}\omega_i^2 + \mathrm{j}r_{ci-1}\dot{\omega}_{i-1} - r_{ci-1}\omega_{i-1}^2 \end{aligned} \tag{17}$$

As seen in Figure 8, the component with index 1 is considered to be connected with a rotational joint to the world frame. In conclusion, (17) for $i = 1$ may be expressed as

$$a_{m1} = \mathrm{j}r_{l1}\dot{\omega}_1 - r_{l1}\omega_1^2 \tag{18}$$

Expressed as vector equation, where every entry corresponds to one component, this leads to

$$\mathbf{A}\vec{\mathbf{a}}_m = \mathrm{j}\mathbf{R}\dot{\vec{\boldsymbol{\omega}}} - \mathbf{R}\vec{\boldsymbol{\omega}}^2 \tag{19}$$

with

$$\mathbf{A} = \begin{bmatrix} 1 & 0 & 0 & .. & .. & .. & 0 \\ -1 & 1 & 0 & & & & : \\ 0 & -1 & 1 & & & & : \\ : & & .. & & & & : \\ : & & & -1 & 1 & 0 & 0 \\ : & & & 0 & -1 & 1 & 0 \\ 0 & .. & .. & 0 & 0 & -1 & 1 \end{bmatrix} \tag{20}$$

$$\mathbf{R} = \begin{bmatrix} r_{l1} & 0 & 0 & .. & .. & .. & 0 \\ r_{c1} & r_{l2} & 0 & & & & : \\ 0 & r_{c2} & r_{l3} & & & & : \\ : & & & .. & & & : \\ : & & & r_{cn-3} & r_{ln-2} & 0 & 0 \\ : & & & 0 & r_{cn-2} & r_{ln-1} & 0 \\ 0 & .. & .. & 0 & 0 & r_{cn-1} & r_{ln} \end{bmatrix} \tag{21}$$

From *Newton-Euler's* law, the acceleration of the i^{th} component [25], for all $i \in [1, .., n-1]$, also follows as

$$m_i a_{mi} = f_{gi} + f_{li} - f_{li+1} \tag{22}$$

As the last chain component with the index n is considered free and only connected to the previous component as seen in Figure 8, (22) for $i = n$ might be expressed as

$$m_n a_{mn} = f_{gn} + f_{ln} \tag{23}$$

(22) and (23) might be expressed as a vector equation as

$$\mathbf{M}\vec{\mathbf{a}}_m = \vec{\mathbf{f}}_g + \mathbf{B}\vec{\mathbf{f}}_l \tag{24}$$

with

$$\mathbf{M} = \mathrm{diag}(m_1, .., m_n) = \begin{bmatrix} m_1 & 0 & .. & 0 \\ 0 & . & & : \\ : & & . & 0 \\ 0 & .. & 0 & m_n \end{bmatrix} \tag{25}$$

$$\mathbf{B} = \begin{bmatrix} 1 & -1 & 0 & & .. & .. & 0 \\ 0 & 1 & -1 & & & & : \\ 0 & 0 & 1 & & & & : \\ : & & & .. & & & : \\ : & & & & 1 & -1 & 0 \\ : & & & & 0 & 1 & -1 \\ 0 & .. & .. & .. & 0 & 0 & 1 \end{bmatrix} \tag{26}$$

Solving (24) for $\vec{\mathbf{f}}_\mathbf{l}$ and (19) for $\vec{\mathbf{a}}_m$, leads to the force acting on the joints expressed as

$$\vec{\mathbf{f}}_l = \mathrm{j}\mathbf{B}^{-1}\mathbf{M}\mathbf{A}^{-1}\mathbf{R}\dot{\vec{\boldsymbol{\omega}}} - \mathbf{B}^{-1}\mathbf{M}\mathbf{A}^{-1}\mathbf{R}\vec{\boldsymbol{\omega}}^2 - \mathbf{B}^{-1}\vec{\mathbf{f}}_g \tag{27}$$

As $\mathbf{B}$,$\mathbf{M}$,$\mathbf{A}$,$\vec{\boldsymbol{\omega}}$ and $\dot{\vec{\boldsymbol{\omega}}}$ are real, they can be seen as scalars to the complex matrix $\mathbf{R}$. Therefore the real and complex part of $\vec{\mathbf{f}}_l$ might be expressed as

$$\mathrm{Re}(\vec{\mathbf{f}}_l) = -\mathbf{B}^{-1}\mathbf{M}\mathbf{A}^{-1}\mathbf{R}_I\dot{\vec{\boldsymbol{\omega}}} - \mathbf{B}^{-1}\mathbf{M}\mathbf{A}^{-1}\mathbf{R}_R\vec{\boldsymbol{\omega}}^2 - \mathbf{B}^{-1}\vec{\mathbf{f}}_{gR} \tag{28}$$

$$\mathrm{Im}(\vec{\mathbf{f}}_l) = \mathbf{B}^{-1}\mathbf{M}\mathbf{A}^{-1}\mathbf{R}_R\dot{\vec{\boldsymbol{\omega}}} - \mathbf{B}^{-1}\mathbf{M}\mathbf{A}^{-1}\mathbf{R}_I\vec{\boldsymbol{\omega}}^2 - \mathbf{B}^{-1}\vec{\mathbf{f}}_{gI} \tag{29}$$

with $\mathbf{R}_R = \mathrm{Re}(\mathbf{R})$, $\vec{\mathbf{f}}_{gR} = \mathrm{Re}(\vec{\mathbf{f}}_g)$ and $\mathrm{R}_I = \mathrm{Im}(\mathbf{R})$, $\vec{\mathbf{f}}_{gI} = \mathrm{Im}(\vec{\mathbf{f}}_g)$ being the real and complex part of $\mathbf{R}$ and $\vec{\mathbf{f}}_g$

Analysing the momenta [26] in the i^{th} component we find

$$I_{mi}\dot{\omega}_i = t_{gi} + (-r_{li}) \times f_{li} + r_{ci} \times (-f_{li+1}) \tag{30}$$

Considering the boundry condition displayed in Figure 8 the force acting on the free link of the last component is zero:

$$f_{ln+1} = 0 \tag{31}$$

Considering two vectors with their complex representatives

$$\vec{\mathbf{p}}_1 = [p_{x1}, p_{y1}, 0]^t \Rightarrow z_1 = p_{x1} + \mathrm{j} \cdot p_{y1} \tag{32}$$

$$\vec{\mathbf{p}}_2 = [p_{x2}, p_{y2}, 0]^t \Rightarrow z_2 = p_{x2} + \mathrm{j} \cdot p_{y2} \tag{33}$$

the cross product might be written as

$$\vec{\mathbf{p}}_1 \times \vec{\mathbf{p}}_2 = \mathrm{Re}(z_1)\mathrm{Im}(z_2) - \mathrm{Im}(z_1)\mathrm{Re}(z_2) \tag{34}$$

Therefore, (30), taking (31) into account, might be written as

$$\begin{aligned} I_{mi}\dot{\omega}_i =& t_{gmi} - \mathrm{Re}(r_{ci})\mathrm{Im}(f_{li+1}) + \mathrm{Im}(r_{ci})\mathrm{Re}(f_{li+1}) \\ & - \mathrm{Re}(r_{li})\mathrm{Im}(f_{li}) + \mathrm{Im}(r_{li})\mathrm{Re}(f_{li}) \end{aligned} \tag{35}$$

To satisfy the constraint of the component with the index n being a free end, (35) for $i = n$ might be expressed as

$$I_{mn}\dot{\omega}_n = t_{gmn} - \mathrm{Re}(r_{ln})\mathrm{Im}(f_{ln}) + \mathrm{Im}(r_{ln})\mathrm{Re}(f_{ln}) \tag{36}$$

(35) and (36) expressed as a vector equation might be written as

$$\mathbf{\Gamma}\dot{\vec{\boldsymbol{\omega}}} = \vec{\mathbf{t}}_{gm} - \mathbf{R}_R^t\vec{\mathbf{f}}_{lI} + \mathbf{R}_I^t\vec{\mathbf{f}}_{lR} \tag{37}$$

with $\vec{\mathbf{f}}_{lI} = \mathrm{Im}(\vec{\mathbf{f}}_l)$ and $\vec{\mathbf{f}}_{lR} = \mathrm{Re}(\vec{\mathbf{f}}_l)$ being complex and real part of $\vec{\mathbf{f}}_l$, $\mathbf{R}^t$ is the transpose of $\mathbf{R}$ and

$$\mathbf{\Gamma} = \mathrm{diag}(I_{m1}, ..., I_{mn}) = \begin{bmatrix} I_{m1} & 0 & .. & 0 \\ 0 & \cdot & & : \\ : & & \cdot & 0 \\ 0 & .. & 0 & I_{mn} \end{bmatrix} \tag{38}$$

Substituting (28) and (29) into (37) leads to the nonlinear differential equation describing the motion of a 2D pendulum chain with n components:

$$\begin{aligned} &(\mathbf{\Gamma} + \mathbf{R}_R^t\mathbf{E}\mathbf{R}_R + \mathbf{R}_I^t\mathbf{E}\mathbf{R}_I)\dot{\vec{\boldsymbol{\omega}}} = \\ &\vec{\mathbf{t}}_{gm} + (\mathbf{R}_R^t\mathbf{E}\mathbf{R}_I - \mathbf{R}_I^t\mathbf{E}\mathbf{R}_R)\vec{\boldsymbol{\omega}}^2 + \mathbf{R}_R^t\mathbf{B}^{-1}\vec{\mathbf{f}}_{gI} - \mathbf{R}_I^t\mathbf{B}^{-1}\vec{\mathbf{f}}_{gR} \end{aligned} \tag{39}$$

with the substitution $\mathrm{E} = \mathbf{B}^{-1}\mathbf{M}\mathbf{A}^{-1}$.

5.2. Numerical simulation

As r_l and r_c are a function of the angle between the component, so is the matrix $\mathbf{R}$. As a result, the non-linear differential equation (39) describes the angular acceleration between the components as a function of angular velocity and the angle. Equation 39 is solvable if the square matrices $\mathbf{B}$ and $(\mathbf{\Gamma}+\mathbf{R}_R^t\mathbf{E}\mathbf{R}_R+\mathbf{R}_I^t\mathbf{E}\mathbf{R}_I)$ are invertible. Under the described constraint, matrix $\mathbf{B}$ is invertible. The left hand side of Equation (39) $(\mathbf{\Gamma} + \mathbf{R}_R^t\mathbf{E}\mathbf{R}_R + \mathbf{R}_I^t\mathbf{E}\mathbf{R}_I)$ is shown in simulation to be invertible for significant cases with $|r_{li}|, |r_{ci}| > 0$ and $r_{li} \neq r_{ci}$. In this work a double *Euler* integration [27] is used to simulate the system dynamics with defined initial conditions $\vec{\boldsymbol{\phi}} = \vec{\boldsymbol{\phi}}_0$, $\vec{\boldsymbol{\omega}} = \vec{\boldsymbol{\omega}}_0$, the matrices $\mathbf{M}$, $\mathbf{\Gamma}$, $\mathbf{E}$, $\mathbf{B}^{-1}$ and time step Δt. The iterative algorithm is described

(i) Calculate matrix $\mathbf{R}(\vec{\boldsymbol{\phi}})$
(ii) Update forces and momenta acting on components $\vec{\mathbf{f}}_g$,$\vec{\mathbf{t}}_{gm}$
(iii) Solve (39) for $\dot{\vec{\boldsymbol{\omega}}}$
(iv) $\vec{\boldsymbol{\omega}} = \vec{\boldsymbol{\omega}} + \Delta t \cdot \dot{\vec{\boldsymbol{\omega}}}$
(v) $\vec{\boldsymbol{\phi}} = \vec{\boldsymbol{\phi}} + \Delta t \cdot \vec{\boldsymbol{\omega}}$
(vi) Collision handling

Figure 9: Pseudo code for the Double-Euler-Integration of Equation 39

in Figure 9.
During the folding process the components might come in contact with each other outside of their joints. No reflection or bouncing was observed upon two components snapping together due to magnetic forces in experiment. Therefore, to compensate for contact physics a simple collision handling was added in every iteration in Figure 9 in step (vi), to approximate impulse transfer between components in contact and prevent overlapping. The collision handling depends on the relative angle between the components $\vec{\boldsymbol{\phi}}_{rel}$, which is computed from the absolute angle $\vec{\boldsymbol{\phi}}$ of all components in respect to the world frame. The unfolded position, as shown in Figure 3, is considered $\phi_{rel\,i} = 0\,\text{rad}$ for $i \in [2, .., n]$. The components i and $i-1$ are considered snapped together if

$$\phi_{rel\,i} > |90\%\,\pi/2\,rad| \tag{40}$$

If condition (40) is satisfied, then the relative angle between component i and $i-1$ is set to $\phi_{rel\,i} = \pi/2$ for $\phi_{rel\,i} > 0$ or $\phi_{rel\,i} = -\pi/2$ for $\phi_{rel\,i} < 0$. Additionally the angular velocity is averaged over both components.

5.3. Error analysis

The algorithm was applied to the 2D folding chain with component one being fixed to the world frame and analysed for its expected error and energy conservation, as well as compared to the a motion tracking of the real system. For a realistic comparison, dynamic friction was introduced based on the *Coulomb* friction model *L. Lazzarotto 1997* [28]. A friction force was

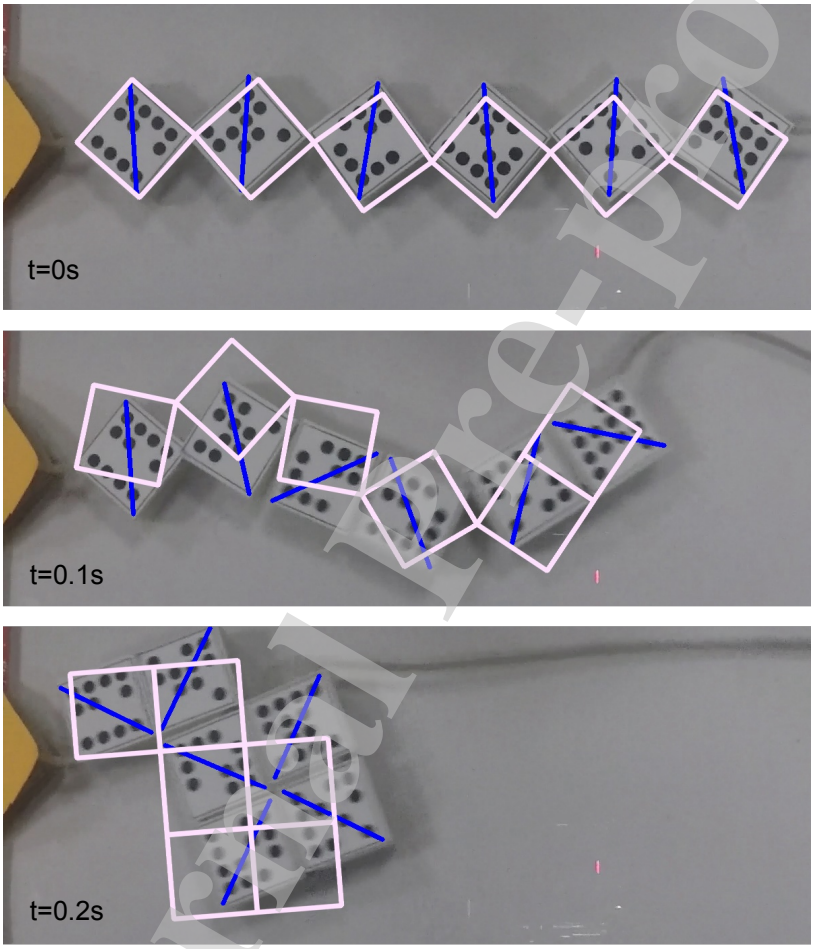

Figure 10: Motion tracking footage of different time steps of modified *free-fold* experiment for sequence 3, with overlay dynamic simulation results. With the left chain end fixed in place and the other chain end free. Diagonal lines are produced by motion tracking. Squares display simulated system response.

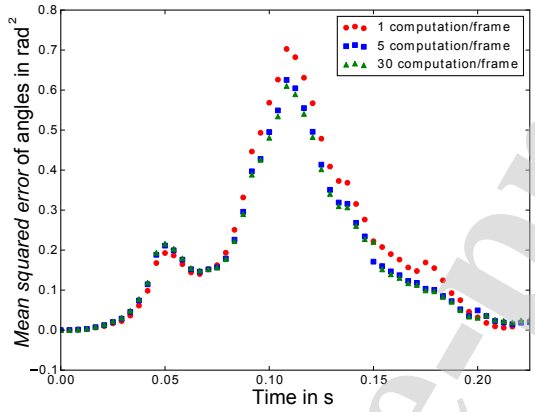

Figure 11: *Mean squared error (MSE)* of the degrees of freedom (angles) over time for different step size $\Delta t = (240 * \text{computations/frame})^{-1}$ s, with $h = 3$ point charges per magnet surface.

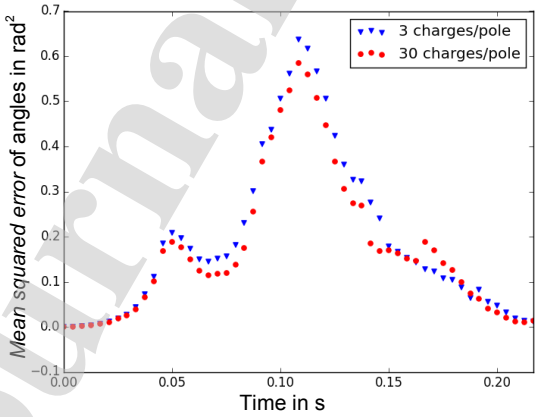

Figure 12: *Mean squared error (MSE)* of degree of freedom (angles) over different number of charges per polarised magnet surface h, with $\Delta t = (240 * 5)^{-1}$ s.

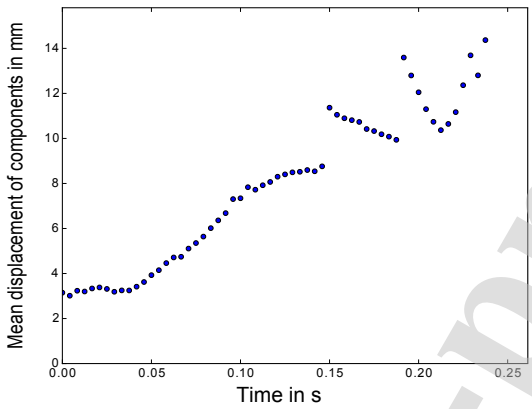

Figure 13: Displacement of the center of mass between simulation and motion tracking of sequence 3 over time, with $\Delta t = (240 * 5)^{-1}$ s. The *Coulomb* friction coefficient $\mu_f = 0.35$ and charge density of $\mathrm{q}_{total} = 17.1892\,\mathrm{Cm}^{-3}$.

introduced to the generalised force equivalent to

$$\vec{\mathbf{f}}_{fric} = -\frac{\vec{\mathbf{v}}_m}{|\vec{\mathbf{v}}_m|}\mu_f \vec{\mathbf{m}} g \tag{41}$$

with $\vec{\mathbf{m}} = (m_1, .., m_i)$.

The friction coefficient of $\mu_f = 0.35$ was adopted using the data of *L. Lazzarotto 1997* [28] and *H.S. Benabdallah 2007* [29]. The static friction in the system was neglected as the dynamic behaviour of the chain was analysed. The folding process of sequence 3 was recorded by a *Hero 4 black* (*GoPro Media Ltd*, UK) camera with a frame rate of 240 frames per second. Position and orientation of each component was detected in each frame, as seen in Figure 10 and compared against simulation results.

Figure 11 shows the *mean squared error* over time for different step sizes Δt. A time step of $\Delta t = (240 * 5)^{-1}$ s was chosen for further computation.

Figure 12 shows the *mean squared error* over time for different number of point charges h per magnet surface. As the difference between $h = 3$ and $h = 30$ is minimal, $h = 3$ represented best computational performance and was chosen for further computation.

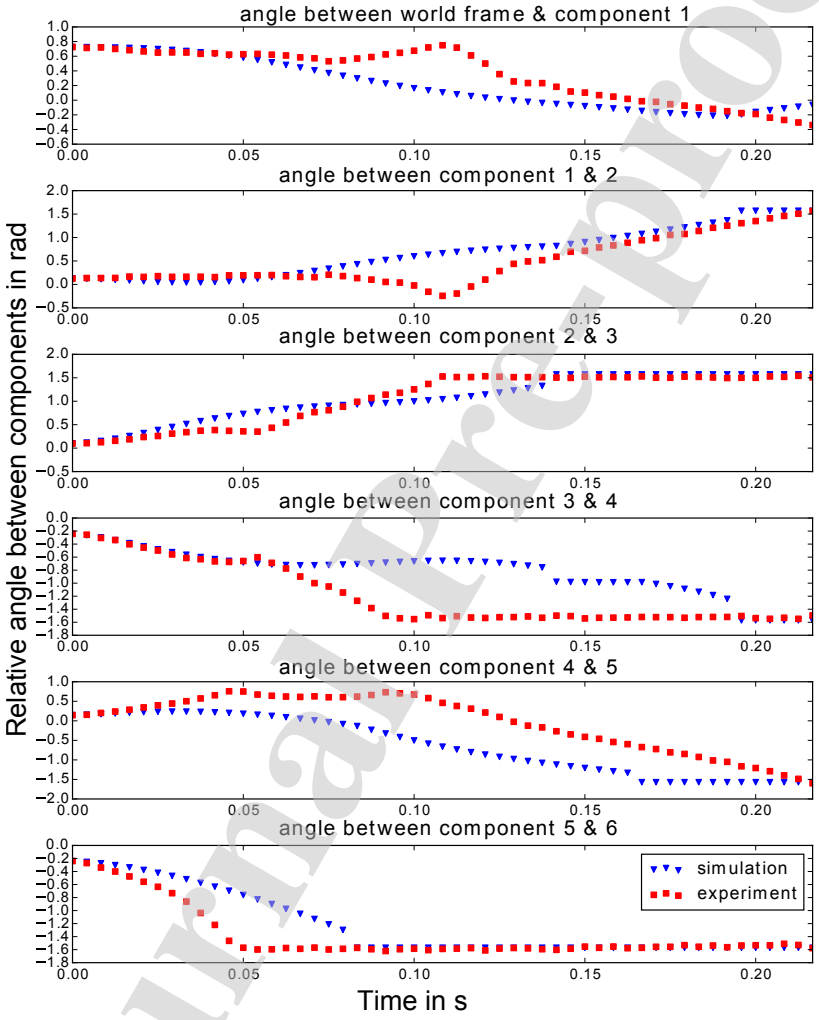

Figure 14: Relative angle compared between simulation and motion tracking, with $\Delta t = (240 * 5)^{-1}$ s, *Coulomb* friction coefficient $\mu_f = 3.5$ and charge density of $q_{total} = 17.1892\,\mathrm{Cm}^{-3}$.

Figure 13 shows the mean displacement between the center of mass in simulation and the tracked components, with an average displacement over all time steps and components of 8.2 mm. Noticeable are the jumps in the mean displacement, due to the previously described collision handling. At time point $t = 0\,\mathrm{s}$, there is a mean displacement of 3 mm between simulation and experiment as the experimental system only approximated hinges and the distance between the components is not constant.

Figure 14 shows the change of the relative angle between the components in simulation compared to the results of the experimental motion tracking. The simulation predicts the final folded shape correctly, with a difference in angle averaged over all time steps and components of 0.442 rad. However as seen in Figure 14, there are small differences between the recorded and simulated movement. The order of components to reach a relative angle of $\pm\pi/2$ is different in simulation. In more complex systems, this could cause a significant difference between the prediction and final folding. However, this was not the case for the system investigated in this work.

One possible reason for this error in prediction could be the constructive simplicity of the experimental setup, approximating a system with hinges and the inevitable error associated with manual priming and triggering of the folding process. Another possible explanation is the error introduced by the approximation of the magnetic forces, using the point charge model.

In order to eliminate the error due to the approximation of magnetic forces and generate a second indicator for the accuracy of the presented algorithm, a non-magnetic, multi-body pendulum was simulated and analysed for preservation of internal energy. The multi-body pendulum consisted of a chain with n components, where one end of the chain is fixed to the world frame and the other is free. The chain is only driven by gravitational forces $\vec{\mathbf{f}}_{ig} = m_i \cdot [0, -\mathrm{g}]^t$ acting on the components, with gravitational constant on earth $\mathrm{g} = 9.8\,\mathrm{m/s^2}$. Friction is neglected and therefore the kinetic and potential energy of such a system has to be constant over time. The kinetic and potential energy sum up to the internal energy of the system and can be computed by equations presented by *A. Jain 2008* [30]. Therefore the change of the systems internal energy between two time points is interpreted as proportional to the maximum possible error introduced by the simulation time step. The simulation was run for 1000 time steps. As seen in Figure 15, the

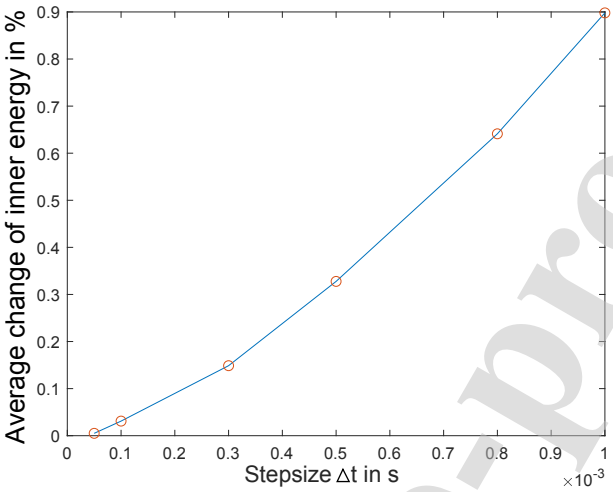

Figure 15: Percentage difference in kinetic- plus potential energy between two time steps, in a pendulum system with 3 components, averaged over 1000 time steps for different time step size Δt.

error of internal energy decreases with a smaller time step size Δt. This leads to the assumption that the numerical integration significantly contributes to the error and the error can be minimised by minimising Δt.

5.4. Computing time

As previously noted, the time efficiency of the prediction algorithm is essential for the folding prediction of long chains. In a comparison between the dynamic simulation and the energy minimisation prediction, it is to be expected that the energy minimisation is faster as it only analyses states of interest instead of time steps and therefore has significantly less states to compute.

For the estimation of computation time efficency of Equation 39 magnetic forces, friction and collision have been removed from simulation. The simulated system to estimate computation time is a pendulum of n components, only agitated by constant gravitational force acting on each component. Simulations with different numbers of chain components were executed in *Python*. All computations were conducted on a *Windows* computer with a *Intel Xeon E5-2678 v3* processor with 2.5 GHz, 12 cores and 16 GB system memory. The Simulation was implemented in *Python* using the *NumPy* library to solve the vector Equation 39.

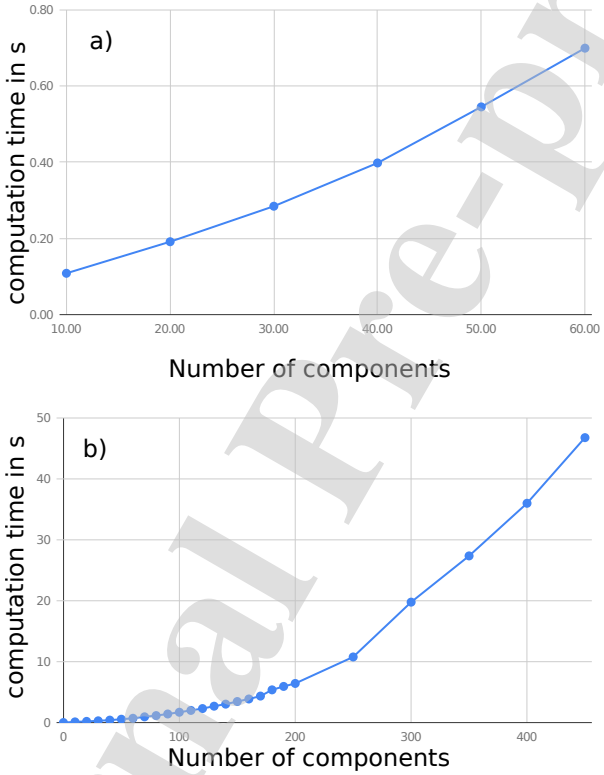

Figure 16: Average computing time over 10 computation cycle, with 1000 time steps each, for various numbers of chain components and degrees of freedom and a) for up to 60 components b) up to 450 components, of the vectorised *Newton-Euler* approach, presented in this paper.

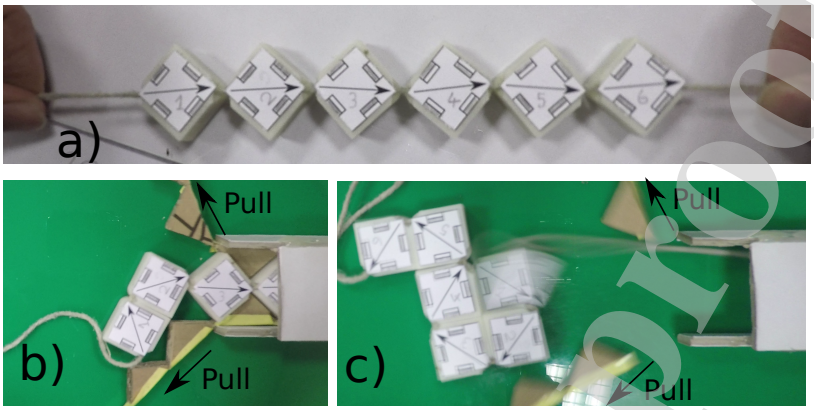

Figure 17: Folding deployment modes on the example of sequence 1. a) Free-fold, b) Forward *tube-feed*: beginning of folding, c) Backward *tube-feed*: end of folding

As seen in Figure 16, the algorithm presented in this paper shows a near linear relationship between number of components and computing time for less than approximately 60 components. For up to 450 components it shows a super-linear relationship between number of components and computation time of approximately $O(n^{1.5})$.

6. Experimental Validation

The system used for the experiments is composed of 3D printed polymer casings seen in Figure 2. Each casing makes up one rigid body in the chain and contains four magnets. The casings are connected with an inelastic string, and fold on a planar, low friction surface due to the forces acting between the magnets. All movement normal to the surface is restricted, whereas the string connection approximates a hinge joint between the casings. Viewed from the top of the plane, as shown in Figure 17, all magnets are fixed with their north side facing either inwards or outwards from the casings side-walls. The chain is defined by the sequence of casing components and how their magnets are oriented. The three sequences shown in Figure 3 were built.

The chain is considered to have folded to a stable state if all relative angles between the components are ± 90 deg and, therefore, at least one face of all

components is in contact with a face of another component and the chain has stopped moving. Due to the friction between the surface and the components, a chain limited to $n = 6$ casing components were used, to enable the analysis of folding error due to friction in relation to the deployment modes of the release.

Each sequence described in Figure 3 was tested under three different conditions of release:

(i) *Free-fold*: The chain was manually pulled apart from start and end and then released simultaneously, so that all components were free to move at the same time. 100 experiments per sequence

(ii) Forward *tube-feed*: The chain was fed component-by-component, out of a rigid tube, starting with the first component in the sequence. The components were kept in neutral position using spacers. The chain was propelled by pulling the spacers manually with a constant speed as seen in Figure 17. 50 experiments per sequence.

(iii) Backward *tube-feed*: The chain was fed component-by-component, out of a rigid tube, starting with the last component in the sequence analogue to the Forward *tube-feed* but in reversed order. 50 experiments per sequence.

6.1. Experimental Results

Figure 18 shows the probability of each sequence folding into their defined stable states, or misfolding for each deployment mode as measured in the experimental setup. The final chain fold is considered a misfold when the components come to a halt before the folding process is complete. The folding process is considered complete when all components are in contact with at least one other component (i.e. surface to surface). The only exception to this is outcome S1E, which is the only occurrence of a conflict in a finished folded shape during the experiments and therefore a small gap exists between components 4 and 5 upon completion of the folding.

As shown in Figure 18, the experiment fully supports the simulation results for sequence 3. Forward *tube-feed* and *free-fold* experiments of sequence 1 and 2 however, have a higher probability to fold into a local minima instead of the global minimum for that sequence. In these cases, the chains fold into the respective shapes with the least lateral movement of the components. While this is predicted by the *tube-feed* simulation for sequence 2, *tube-feed*

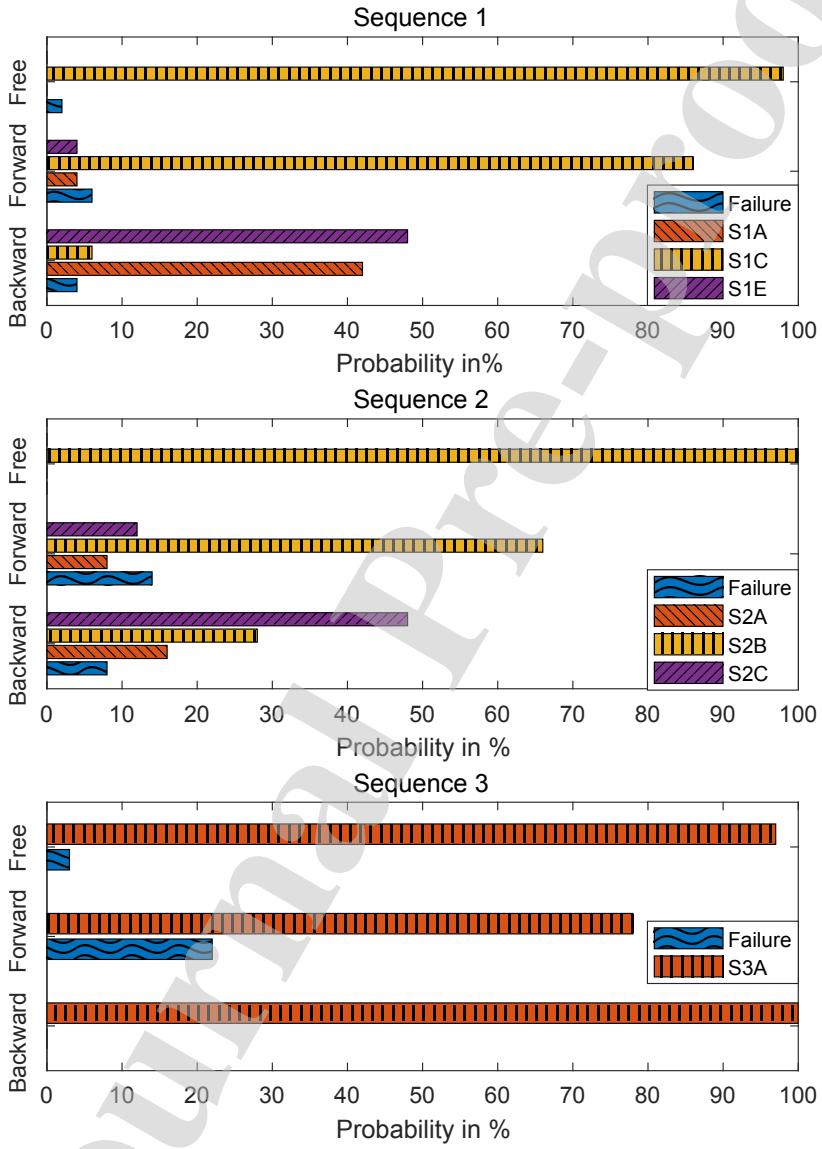

Figure 18: Probability of each chain sequence and deployment mode to fold into predicted shapes displayed in Figure 7 or misfold, as measured during experiment.

simulation fails to predict the folding of sequence 1. The backward *tube-feed* experiment for both sequence 1 and 2 show near equal probability of folding for multiple shapes and therefore cannot be compared to prediction.
It is noteworthy that sequences 1 and 2 have high probability to fold into different shapes depending on the deployment modes of the release, whereas sequence 3 preferentially folds into only one shape. All other possible folds of sequence 3 would result in two magnets meeting with the same polarisation and thus repelling each other. Nevertheless, the deployment modes of deployment also have a measurable influence on the probability of a misfold of sequence 3. In the case of S3A, components 5 and 6 are connected to components 3 and 4. This requires, that component 5 is dragging component 6 along during the *free-fold* and forward *tube-feed* experiments. The resulting friction force, gives rise to a misfold.

For *tube-feed* systems, the force used to push the chain out of the tube can be seen as a driving force [12] of the system and can promote the fold into a lower or higher internal free energy state. However the direction of deployment of the chain out of the tube also has a significant influence. It follows that only certain driving forces promote some folded shapes. For example, the backwards deployment of sequence 1 gives nearly the same probability to fold into shape S1A as into S1C with a much lower probability to fold into shape S1B compared to the forward deployment.

7. Discussion

Comparing the experimental results to the energy minimisation prediction shows that the chain, in the absence of a misfold, will fold into one of the stable states. Clearly the deployment modes have a significant effect on the folding of the chain. The folding of sequence 1 and sequence 2 supports the hypothesis that in *free-fold*, the chain tends to fold into a shape that requires the least movement for each component, even if the resulting shape is not the global minimum of internal energy. Sequence 1 however, shows one more stable and one conflicting result at a lower *Coulomb* energy than folding shape S1C, as seen in Figure 19. It is assumed that shape S1E was experimentally unfavourable due to the wire exiting component 1.

Minimising the energy for only one degree of freedom at a time (component-by-component), the energy minimisation prediction can predict the result of some *tube-feed* folding experiments. However experiments where the different resulting shapes have nearly the same probability of occurring are not predictable by the energy minimisation method. The energy minimisation prediction in its basic application presented in this paper does not take the initial shape into account and therefore cannot compensate for different starting conditions of the fold. Nor can it account for a mis-fold as the energy minimisation neglects the dynamics of the folding process, only analysing states of interest. In conclusion, the comparison between the energy optimisation and experiment shows that the energy minimisation can be used to carefully plan a shape to support only one stable state and reliably fold into the desired shape, depending on the deployment mode and constraints. However energy minimisation cannot reliably predict the folding of a complex chain with multiple stable states under all possible deployment modes and constraints, due to its neglecting chain dynamics.

Depending on the use case, a number of unknown factors might influence the folding of a chain and therefore introduce an error in the folding prediction. For this simple setup, these influences are the human error during the resetting and execution of the experiments, resulting in different folds for the same chain under the same release conditions. A second source of error is the difference between the real chain in experiment and the idealised chain in simulation. Extrapolating this behaviour for longer, more complex chains, it is to be expected that the unpredictability for folding will rise with the length of the chain.

In summary, energy minimisation approaches alone cannot account for error sources and an analysis of the systems dynamics is necessary. The algorithm to compute the dynamics of the system, presented in this paper, is specialized for chains and allows the folding prediction for long chains as well as the complex relationships of forces between the components. The algorithm is largely expressed in a set of vector equations governing the dynamic behaviour of the simulated system. These vector equations use square matrices and therefore, the number of operations to solve the equations has a square relationship to the number of components in the chain. However, the vectorisation allows for a convenient implementation with vector computation library, such as the here used NumPy library[31], that make full use of parallel computation architecture. As Figure 16 shows this results in a near linear relationship between number of components and computation time.

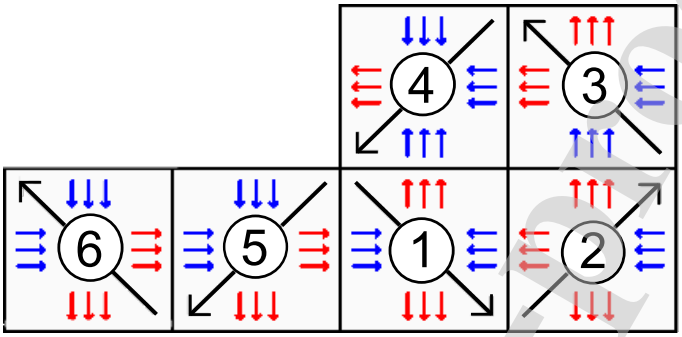

a) S1B with Coulomb energy score of -25.6527

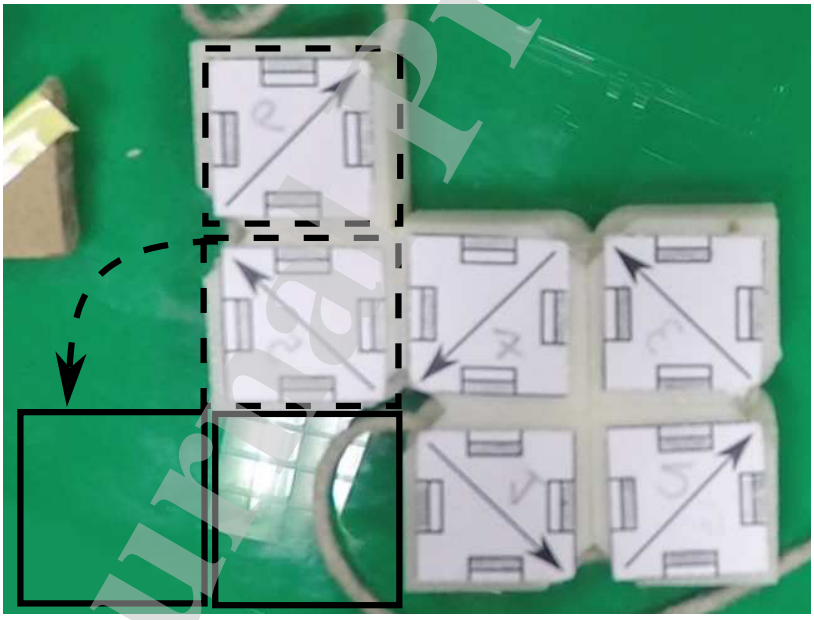

b) S1A with Coulomb energy score of -25.8098

Figure 19: a) Folding S1B, not occurring in experiment. b) favourable fold S1A, highlighting differences in folding shapes.

However there is a limit of possible simultaneous operations in a computer system and for more than approximately 60 components the relationship exasperates. Considering the previously described sources of error, the results from experiment in this paper indicate that the proposed algorithm is capable of near-accurate simulation of the dynamics of a 2D chain, on a millisecond scale. Furthermore, it is to be assumed that the differential equation 39 is energy preserving as it directly follows from the Newton-Euler equations and that the small change in the internal energy occurring from this algorithm originates from the integration method. However the comparison of the dynamics simulation to the experimental results show some differences. With more unknown variables in the system these differences may be expected to rise.

The novel dynamics algorithm is derived under the assumption of planar movement only. As such, *Newton-Euler* Equations (1,2) simplify to Equations (1,3). The Algorithm was derived from the 2D case of the *Newton-Euler* equations and only allows for planar rotation and the introduction of complex numbers further simplifies the handling of rotations. This allows for the separate Equations (19), (24) and (37) to be combined and rearranged into equation (39). In a 3D case, these assumptions and conveniences are not applicable and a combination of all three formulae proves more challenging. Quaternions similar to complex numbers allow for a convenient representation of rotation in 3D but are not commutative. Furthermore it can not be guaranteed that matrix B is invertible for all possible constraints. However the in this paper analysed case represent an important problem in robotics in 2D i.e., to efficiently calculate the forward dynamics of a serial chain of rigid bodys, with one end fixed to the world frame and the other free. The algorithm needs to be translated to 3D to fully address this problem but its potential is proven here to be a conveniently implemented algorithm to significantly speed up computation time for a class of self-folding chains, utilising parallel computation architectures.

8. Future Work

Even though both presented prediction methods of a folding chain were proven to be able to predict the folding of most chains, neither approach is able to predict the folding under all possible circumstances. A future synthesis of both approaches may compensate for these shortcomings and enable a

more efficient and accurate prediction of the folding of a chain.
The differential equation describing the dynamics so far only supports a specific set of constraints. Different constraints need to be explored. Furthermore the error of the *Euler* integration is proportional to the speed of the components. A better integration method might be implemented to solve the non-linear differential equation and lower the resulting error.
The variant of the *Newton-Euler* approach presented in this paper, should be translated to 3D, in order to enable a simulation of meaningful physical systems. The use of quaternions to represent 3D coordinates, could enable the folding dynamics to be described in a similar approach to that presented in this work.

9. Funding

Pádraig Cantillon-Murphy and Tim H. Fass are supported by Science Foundation Ireland career development award 17/CDA/4771.

References

[1] S. T. Griffith, J. Jacobson, Growing Machines, Ph.D. thesis, Massachusetts Institute of Technology (2004).

[2] S. M. Felton, M. T. Tolley, B. Shin, C. D. Onal, E. D. Demaine, D. Rus, R. J. Wood, Self-folding with shape memory composites, Soft Matter 9 (32) (2013) 7688–7694. doi:10.1039/c3sm51003d.

[3] K. Noonan, D. O'Brien, J. Snoeyink, Probik: Protein Backbone Motion by Inverse Kinematics, The International Journal of Robotics Research 24 (11) (2005) 971–982. doi:10.1177/0278364905059108.

[4] B. An, D. Rus, Designing and programming self-folding sheets, Robotics and Autonomous Systems 62 (7) (2014) 976–1001. doi:10.1016/j.robot.2013.06.015.

[5] K. Zimmermann, V. A. Naletova, I. Zeidis, V. A. Turkov, E. Kolev, M. V. Lukashevich, G. V. Stepanov, A deformable magnetizable worm in a magnetic field-A prototype of a mobile crawling robot, Journal of Magnetism and Magnetic Materials 311 (1 SPEC. ISS.) (2007) 450–453. doi:10.1016/j.jmmm.2006.11.153.

[6] S. Yim, M. Sitti, SoftCubes: Stretchable and self-assembling three-dimensional soft modular matter, International Journal of Robotics Research 33 (8) (2014) 1083–1097. doi:10.1177/0278364914527630.

[7] R. P. McEvoy, M. McMenamin, G. Ha, J. H. Lang, P. Cantillon-Murphy, Self-deployed magnetic polygons: Design, construction, and application, IEEE Transactions on Magnetics 49 (1) (2013) 496–505. doi:10.1109/TMAG.2012.2205935.

[8] J. Tugwell, P. Brennan, C. O'Shea, K. O'Donoghue, T. Power, M. O'Shea, J. Griffiths, R. Cahill, P. Cantillon-Murphy, Electropermanent magnetic anchoring for surgery and endoscopy, IEEE Transactions on Biomedical Engineering 62 (3) (2015) 842–848. doi:10.1109/TBME.2014.2366032.

[9] L. Adelman, Towards a mathematical therory of self assembly (extended abstract), Tech. rep., University of Southern California, Los Angeles (1999). doi:10.1.1.41.685.

[10] R. Featherstone, Robot dynamics algorithms, Vol. 25, 1989. doi:10.1016/0005-1098(89)90037-x.

[11] P. Moubarak, P. Ben-Tzvi, Modular and reconfigurable mobile robotics, Robotics and Autonomous Systems 60 (12) (2012) 1648–1663. doi:10.1016/j.robot.2012.09.002.

[12] J. A. Pelesko, Self Assembly. The Science of Things That Put Themselves Together., Chapman and Hall/CRC, 2007. doi:10.1002/anie.200885572.

[13] T. J. Brunette, O. Brock, Improving protein structure prediction with model-based search, Bioinformatics 21 (1) (2005) i66–i74. doi:10.1093/bioinformatics/bti1029.

[14] W. M. Silver, On the Equivalence of Lagrangian and Newton-Euler Dynamics for Manipulators, The International Journal of Robotics Research 1 (2) (1982) 60–70. doi:10.1177/027836498200100204.

[15] B. Mirtich, Impulse-based Dynamic Simulation of Rigid Body Systems, Ph.D. thesis (1996).

[16] D. Naishlos, M. Biberstein, S. Ben-David, A. Zaks, Vectorizing for a SIMdD DSP architecture, CASES 2003: International Conference on Compilers, Architecture, and Synthesis for Embedded Systems (2003) 2–11doi:10.1145/951713.951714.

[17] R. Featherstone, Divide-and-conquer articulated-body algorithm for parallel O(log(n)) calculation of rigid-body dynamics. Part 1: Basic algorithm, International Journal of Robotics Research 18 (9) (1999) 867–875. doi:10.1177/02783649922066619.

[18] K. Chadaj, P. Malczyk, J. Fraczek, A parallel recursive hamiltonian algorithm for forward dynamics of serial kinematic chains, IEEE Transactions on Robotics 33 (3) (2017) 647–660. doi:10.1109/TRO.2017.2654507.

[19] A. Stokes, R. Brockett, Dynamics of kinematic chains, International Journal of Robotics Research 15 (4) (1996) 393–405. doi:10.1177/027836499601500406.

[20] P. C. Müller, Robot dynamics and control, Automatica 28 (3) (1992) 655–656. arXiv:arXiv:1011.1669v3, doi:10.1016/0005-1098(92)90197-N.

[21] R. Lathrop, Parallelism in manipulator dynamics, in: Proceedings. 1985 IEEE International Conference on Robotics and Automation, Vol. 2, Institute of Electrical and Electronics Engineers, 1985, pp. 772–778. doi:10.1109/ROBOT.1985.1087228.

[22] F. C. Park, J. E. Bobrow, S. R. Ploen, A Lie group formulation of robot dynamics, The International Journal of Robotics Research 14 (6) (1995) 609–618. doi:10.1177/027836499501400606.

[23] E. Furlani, Permanent Magnet and Electromechanical Devices, Elsevier, 2001. doi:10.1016/B978-0-12-269951-1.X5000-1.

[24] J. Y. S. Luh, M. W. Walker, R. P. C. Paul, On-Line Computational Scheme for Mechanical Manipulators, Journal of Dynamic Systems, Measurement, and Control 102 (2) (1980) 69. doi:10.1115/1.3149599.

[25] M. D. Ardema, Newton-Euler Dynamics, Springer US, 2005. arXiv:1011.1669, doi:10.1007/b101082.

[26] F. E. Udwadia, P. Phohomsiri, Explicit equations of motion for constrained mechanical systems with singular mass matrices and applications to multi-body dynamics, Proceedings of the Royal Society A: Mathematical, Physical and Engineering Sciences 462 (2071) (2006) 2097–2117. doi:10.1098/rspa.2006.1662.

[27] E. Hairer, S. P. Nørsett, G. Wanner, Solving ordinary differential equations I. nonstiff problems, Mathematics and Computers in Simulation 29 (5) (1987) 447. arXiv:arXiv:1011.1669v3, doi:10.1016/0378-4754(87)90083-8.

[28] L. Lazzarotto, L. Dubar, A. Dubois, P. Ravassard, J. Oudin, Identification of Coulomb's friction coefficient in real contact conditions applied to a wire drawing process, Wear Jouranl 211 (1) (1997) 54–63. doi:10.1016/S0043-1648(97)00080-X.

[29] H. S. Benabdallah, Static friction coefficient of some plastics against steel and aluminum under different contact conditions, Tribology International 40 (1) (2007) 64–73. doi:10.1016/j.triboint.2006.02.031.

[30] A. Jain, Robot and Multibody Dynamics, Springer US, 2011. doi:10.1007/978-1-4020-8600-7.

[31] NumPy-developers, Numpy library (2020).
URL `https://numpy.org/`

Tim H. Fass is a PhD candidate at University College Cork and a member of the Tyndall National Institute in the Biomedical Research laboratory lead by Dr. Pádraig Cantillon-Murphy. Tim H. Fass work focuses on the application of self-assembly for novel medical technologies.

He obtained his Masters in Engineering Science at the TU-Berlin, with a specialization in robotics and material science. He researched in cooperation with the Koç University in Istanbul (2011) and the University of Tokyo (2012) and worked in the Robotics and Biology Laboratory of the TU-Berlin (2015-2016).

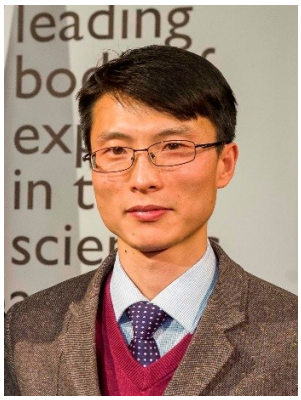

Dr. Guangbo Hao is a Senior Lecturer with University College Cork. He obtained his PhD degree in Mechanical Engineering from Heriot-Watt University in 2011. He is a member of ASME and an elected member of the ASME Mechanisms and Robotics Committee. He is serving as the Editor-in-Chief of the IFToMM affiliated journal: Mechanical Sciences. He has been the regular reviewers in more than 30 top-tier journals such as IEEE and ASME Transactions. He has received the 2017 and 2018 ASME Compliant Mechanisms Awards in a row. He has published over 120 peer-reviewed publications.

Dr. Pádraig Cantillon-Murphy is Senior Lecturer in Electrical and Electronic Engineering at University College Cork, Ireland, academic member of Tyndall National Institute at University College Cork, and an honorary faculty at l'Institut de Chirurgie Guidée par l'Image in Strasbourg. He is principal investigator at the Biomedical Design Laboratory at UCC and Tyndall National Institute which explores novel device development in image-guided surgery and endoscopy. His current research interests include magnets for surgery, electromagnetic tracking and navigation and surgical robotics. He is a former Marie Curie fellow (2010-2014), a former MIT Whitaker fellow (2007-08), and a senior member of the IEEE. He has co-founded two start-up companies and is co-inventor on 6 patent applications.

Author declaration

[Instructions: Please check all applicable boxes and provide additional information as requested.]

1. Conflict of Interest

Potential conflict of interest exists:

We wish to draw the attention of the Editor to the following facts, which may be considered as potential conflicts of interest, and to significant financial contributions to this work:

The nature of potential conflict of interest is described below:

☒No conflict of interest exists.

We wish to confirm that there are no known conflicts of interest associated with this publication and there has been no significant financial support for this work that could have influenced its outcome.

2. Funding

☒Funding was received for this work.

All of the sources of funding for the work described in this publication are acknowledged below:

Pádraig Cantillon-Murphy and Tim H. Fass are supported by Science Foundation Ireland career development award 17/CDA/4771.

☐No funding was received for this work.

3. Intellectual Property

☒We confirm that we have given due consideration to the protection of intellectual property associated with this work and that there are no impediments to publication, including the timing of publication, with respect to intellectual property. In so doing we confirm that we have followed the regulations of our institutions concerning intellectual property.

4. Research Ethics

☒We further confirm that any aspect of the work covered in this manuscript that has involved human patients has been conducted with the ethical approval of all relevant bodies and that such approvals are acknowledged within the manuscript.

☐IRB approval was obtained (required for studies and series of 3 or more cases)

☐Written consent to publish potentially identifying information, such as details or the case and photographs, was obtained from the patient(s) or their legal guardian(s).

5. Authorship

The International Committee of Medical Journal Editors (ICMJE) recommends that authorship be based on the following four criteria:

1. Substantial contributions to the conception or design of the work; or the acquisition, analysis, or interpretation of data for the work; AND

2. Drafting the work or revising it critically for important intellectual content; AND

3. Final approval of the version to be published; AND

4. Agreement to be accountable for all aspects of the work in ensuring that questions related to the accuracy or integrity of any part of the work are appropriately investigated and resolved.

All those designated as authors should meet all four criteria for authorship, and all who meet the four criteria should be identified as authors. For more information on authorship, please see http://www.icmje.org/recommendations/browse/roles-and-responsibilities/defining-the-role-of-authors-and-contributors.html#two.

☒All listed authors meet the ICMJE criteria. ☐We attest that all authors contributed significantly to the creation of this manuscript, each having fulfilled criteria as established by the ICMJE.

☐One or more listed authors do(es) not meet the ICMJE criteria.

We believe these individuals should be listed as authors because:

[Please elaborate below] □

☒We confirm that the manuscript has been read and approved by all named authors.

☒We confirm that the order of authors listed in the manuscript has been approved by all named authors.

6. Contact with the Editorial Office

The Corresponding Author declared on the title page of the manuscript is:

[Insert name below]

☒This author submitted this manuscript using his/her account in EVISE.

☒We understand that this Corresponding Author is the sole contact for the Editorial process (including EVISE and direct communications with the office). He/she is responsible for communicating with the other authors about progress, submissions of revisions and final approval of proofs.

☒We confirm that the email address shown below is accessible by the Corresponding Author, is the address to which Corresponding Author's EVISE account is linked, and has been configured to accept email from the editorial office of American Journal of Ophthalmology Case Reports:

[Insert email address you wish to use for communication with the journal here]

☐Someone other than the Corresponding Author declared above submitted this manuscript from his/her account in EVISE:

[Insert name below]

☐We understand that this author is the sole contact for the Editorial process

(including EVISE and direct communications with the office). He/she is responsible for communicating with the other authors, including the Corresponding Author, about progress, submissions of revisions and final approval of proofs.

We the undersigned agree with all of the above.

	Author's name (Fist, Last)	Signature	Date
1.	Tim H., Fass	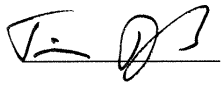	21.10.2019
2.	Guangbo Hao	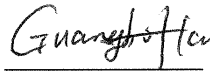	21/10/2019
3.	Padraig Cantillon-Murphy		21/10/2019
4.			
5.			
6.			
7.			
8.			
9.			
10.			